

East Tennessee State University

Digital Commons @ East Tennessee State University

ETSU Faculty Works

Faculty Works

8-1-2020

Object-Based Image Analysis of Ground-Penetrating Radar Data for Archaic Hearths

Reagan L. Cornett

East Tennessee State University

Eileen G. Ernenwein

East Tennessee State University, ernenwei@etsu.edu

Follow this and additional works at: <https://dc.etsu.edu/etsu-works>

Citation Information

Cornett, Reagan L.; and Ernenwein, Eileen G.. 2020. Object-Based Image Analysis of Ground-Penetrating Radar Data for Archaic Hearths. *Remote Sensing*. Vol.12(16). <https://doi.org/10.3390/RS12162539>

This Article is brought to you for free and open access by the Faculty Works at Digital Commons @ East Tennessee State University. It has been accepted for inclusion in ETSU Faculty Works by an authorized administrator of Digital Commons @ East Tennessee State University. For more information, please contact digilib@etsu.edu.

Object-Based Image Analysis of Ground-Penetrating Radar Data for Archaic Hearths

Copyright Statement

© 2020 by the authors. Licensee MDPI, Basel, Switzerland. This article is an open access article distributed under the terms and conditions of the Creative Commons Attribution (CC BY) license (<http://creativecommons.org/licenses/by/4.0/>).

Creative Commons License



This work is licensed under a [Creative Commons Attribution 4.0 International License](https://creativecommons.org/licenses/by/4.0/).

Article

Object-Based Image Analysis of Ground-Penetrating Radar Data for Archaic Hearths

Reagan L. Cornett and Eileen G. Ernenwein * 

Department of Geosciences, East Tennessee State University, Johnson City, TN 37614, USA; zrlc5@etsu.edu

* Correspondence: ernenwei@etsu.edu

Received: 20 June 2020; Accepted: 4 August 2020; Published: 7 August 2020



Abstract: Object-based image analysis (OBIA) has been increasingly used to identify terrain features of archaeological sites, but only recently to extract subsurface archaeological features from geophysical data. In this study, we use a semi-automated OBIA to identify Archaic (8000–1000 BC) hearths from Ground-Penetrating Radar (GPR) data collected at David Crockett Birthplace State Park in eastern Tennessee in the southeastern United States. The data were preprocessed using *GPR-SLICE*, *Surfer*, and *Archaeofusion* software, and amplitude depth slices were selected that contained anomalies ranging from 0.80 to 1.20 m below surface (BS). Next, the data were segmented within *ESRI ArcMap* GIS software using a global threshold and, after vectorization, classified using four attributes: area, perimeter, length-to-width ratio, and Circularity Index. The user-defined parameters were based on an excavated Archaic circular hearth found at a depth greater than one meter, which consisted of fire-cracked rock and had a diameter greater than one meter. These observations were in agreement with previous excavations of hearths at the site. Features that had a high probability of being Archaic hearths were further delineated by human interpretation from radargrams and then ground-truthed by auger testing. The semi-automated OBIA successfully predicted 15 probable Archaic hearths at depths ranging from 0.85 to 1.20 m BS. Observable spatial clustering of hearths may indicate episodes of seasonal occupation by small mobile groups during the Archaic Period.

Keywords: archaeology; archeological prospection; near-surface geophysics; object-based image analysis; remote sensing

1. Introduction

Geophysical techniques are a noninvasive way to map and identify buried archaeological features. Their development has both paralleled and been enhanced by the evolution of geospatial and computer technologies, including GIS and Global Navigation Satellite Systems (GNSS) [1]. In 1999, Joseph Puyol-Gruart [2] wrote that ‘Artificial intelligence is especially useful for experience-based knowledge’, successfully predicting the future importance of digitizing multimedia information in the field of archaeology. Puyol-Gruart [2] further discussed extracting information from databases containing preprocessed data and computer models to identify patterns, while emphasizing the need for validation from a human expert. Semi-automated image analysis has become a multidisciplinary technique that began with aerial photography in the 1960s and satellite imagery in the 1970s. It has been employed in such fields as environmental science, microbiology, and medical imagery using pixel-based and object-based classification algorithms [3–5]. Pixel-based image analysis (PBI) groups pixels based on spectral data values and was first implemented in the 1970s, predating object-based image analysis (OBIA) [3–5]. The OBIA approach utilizes both spectral and spatial data, using a two-step process to segment data based on the spectral values of pixels and then to classify objects based on user-defined spatial attributes [3]. This can be accomplished within geospatial software using computer-implemented algorithms [3]. Case studies comparing the two imagery analysis methods have shown significant

advantages of using OBIA over PBIAs, as OBIA allows for the addition of multi-parameter classifications, while additionally performing better with higher resolution data [4,6–11].

Archaeologists have been using aerial photography to identify archaeological sites and features for over a century and now have access to high-resolution multispectral, light detection and ranging (LiDAR), and synthetic aperture radar (SAR) data from a variety of aerial and spaceborne platforms [10,12,13]. Many recent studies have implemented semi-automated shape factor analysis (object-based) to identify natural terrain features such as sinkholes from LiDAR-derived Digital Elevation Models (DEM) by using ‘form-defining properties’ [14] such as perimeter, area, circularity index, and length-to-width (L2W) ratios (e.g., [15–20]). This technique has been applied in the field of archaeology to detect subtle terrain features such as earthen mounds using semi-automated OBIA with similar parameters (e.g., [10,12,21–24]). OBIA has also been used to map and delineate archaeological features based on their surface expression in multispectral satellite imagery [25]. Davis [21] presents a detailed history of the use of OBIA (coined as ‘GEOBIA’ by Hay and Castilla [26] when applied to remote sensing in the field of geosciences), noting that this method has only been employed in archaeology relatively recently and very rarely in North America. By using semi-automated OBIA to examine remote sensing data, unknown archaeological sites and features can be identified from large datasets, saving time, resources, and possibly the sites themselves from destructive anthropogenic and natural events [12,22].

Several studies have implemented an automated exploration of subsurface features using geophysical data to delineate homogenous objects, including archaeological features. Neural network classification, normalized cross-correlation, clustering, edge-detection segmentation, and supervised and unsupervised classification have been explored (e.g., [3,27–32]). There are few examples in the literature, however, that apply a semi-automated OBIA approach to geophysical data in the field of archaeology. A handful of studies have successfully implemented OBIA using magnetometry data to identify archaeological features (e.g., [3,33–35]), while fewer have applied this to Ground-Penetrating Radar (GPR) data (e.g., [3,36,37]).

In this study, we show that GPR data is highly suited for semi-automated OBIA due to the ability to record features at high spatial resolution and a range of depths. We demonstrate this at a prehistoric site in the southeastern United States where the deepest archaeological features were Archaic (8000–1000 BC) hearths detected with GPR, but out of reach for magnetometry. We also demonstrate the importance of human interpretation in the OBIA process, in agreement with several others [10,38,39], and stress that successful outcomes depend on data quality, the scale and homogeneity of features, and the nature of the site itself [10].

1.1. Study Area

David Crockett Birthplace State Park (Figure 1) is named for the famous Tennessee statesman and frontiersman, and is home to a multicomponent archaeological site whose Native American occupancy dates back to at least the Archaic Period [40,41]. The property rests on two alluvial terraces and a narrow floodplain containing natural springs and is located at the confluence of the Nolichucky River and Big Limestone Creek in Greene County, Tennessee (TN). The park is located in the Middle Nolichucky River Valley of the Valley and Ridge physiographic province, formed by erosion of Cambrian and Ordovician aged dolomite, limestone, and shale bedrock [42,43]. The headwaters of the Nolichucky River are found in the adjacent Blue Ridge physiographic region of North Carolina. The river carries sediments eroding from quartzite, sandstone, basalt, arkose, greywacke, and micaceous shale, which make up the Appalachian Mountains of this region that were formed during the Cambrian and Pre-Cambrian Periods [42,43]. The elevation of the park ranges from 407 to 426 m AMSL (1335–1400 ft AMSL), and the soil type within the survey area consists of a micaceous Congaree fine sandy loam [44].

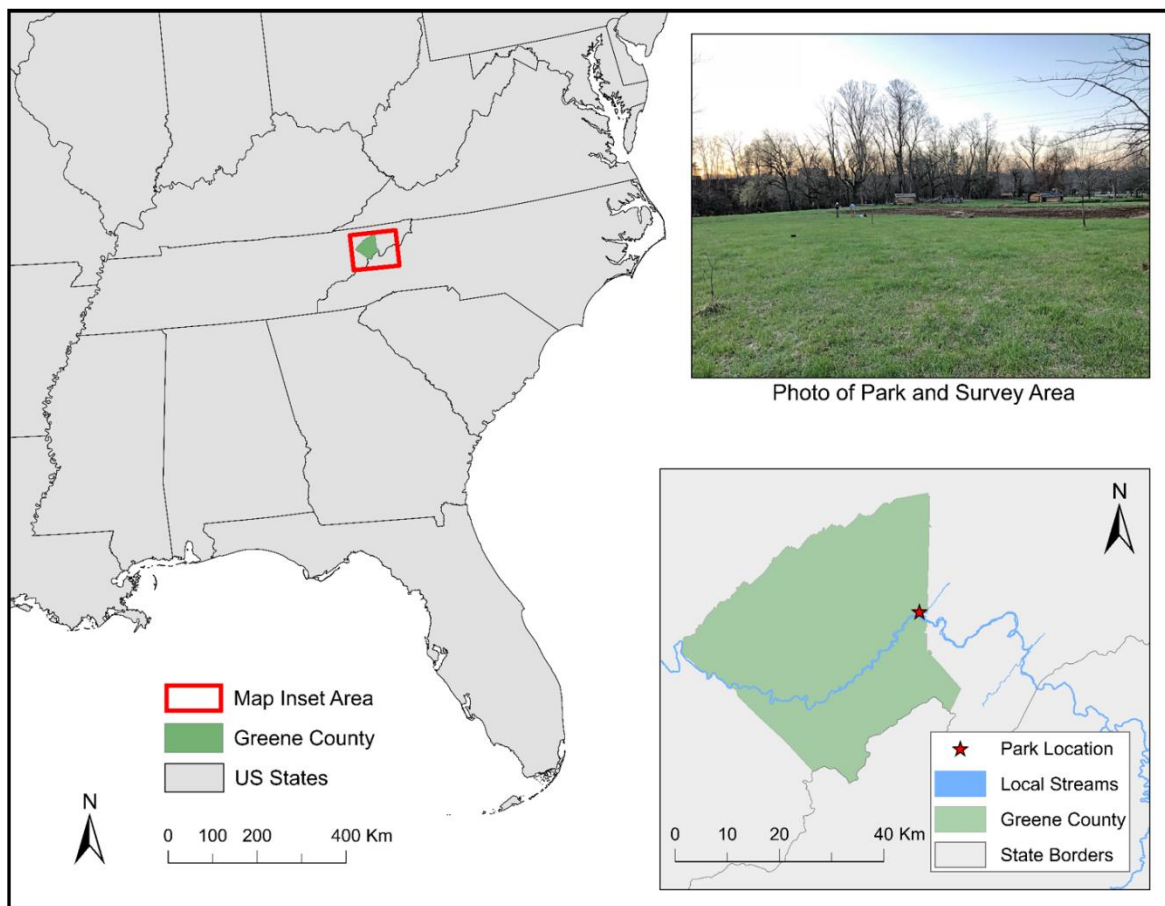


Figure 1. Location of study area, showing David Crockett Birthplace State Park in Greene County, Tennessee (TN), USA, and a photo depicting a portion of the geophysical survey area.

1.2. Archaic Period in the Southeastern United States

Indigenous populations have been in the southeastern US for at least 15,000 years, and archaeologists have divided this time into specific periods based on technological advances and cultural changes as follows: Paleoindian (before 8000 BC), Archaic (8000–1000 BC), Woodland (1000 BC to AD 1000), Mississippian (AD 1000–1570), and Protohistoric (AD 1570–1700) [45–47]. The Archaic Period in the southeastern US is characterized by cultural adaptations to both climate and landscape changes during the early and middle Holocene epoch [48]. It is further delineated into Early (8000–6000 BC), Middle (6000–3000 BC), and Late (3000–1000 BC) Archaic Periods [46,47]. Expanding deciduous forests created an ecosystem rich with nut-bearing trees, seed-bearing plants, and small game, while riverine and marine environments provided an abundance of fish and shellfish [46,47]. The archaeological record has shown that populations increased and that groups were highly mobile across the landscape with a focus on seasonal resource procurement [47]. Major technological changes included smaller projectile points, more expedient stone tools, steatite carved vessels, and domestic plant cultivation [46,47]. Certain cultural traits of the southeastern Archaic Period seem to be regionally localized such as earthen mounds, coastal shell middens, fiber-tempered pottery, and mortuary sites [48–51]. Seven additional Archaic sites have been recorded within a one-mile radius of the study area [52,53].

1.3. Ground-Penetrating Radar for Archaeology

GPR is an active geophysical technique that propagates electromagnetic waves into the subsurface and records reflections from buried interfaces and objects [54,55]. The GPR unit measures the reflection

of returning waves from buried features and anomalies that can be metallic or non-metallic [54]. Reflection magnitude is measured in decibels (db), while velocity is measured in nanoseconds per meter (ns/m) [56]. GPR can also detect changes in soil and sediment properties including areas that have been disturbed by human occupation, making it highly suitable for archaeology [54,55]. Archaeologists utilize GPR to detect the remnants of architectural features, hearths, middens, graves, and even subtle features such as compaction that might not be detected during an excavation [54]. Depth range is potentially increased with lower antenna frequency, which can range from 12.5 to 2600 MHz [57,58]. Ground moisture and sediment type also affect signal penetration [54,55]. Drier sediments and low conductivity sediment types such as sand allow the signal to penetrate up to 30 m below surface (BS), while wetter sediments and materials with a higher conductivity can decrease signal depth to less than one meter [57–59]. Most archaeological GPR studies use antennas ranging from 100 to 900 MHz, typically penetrating up to 5 m below the ground surface. The quality of results varies as ground moisture can change daily, while sediment characteristics are based on geological morphology that may drastically change across a small area [54].

GPR and other geophysical techniques have become essential and often primary methods for mapping, investigating, and understanding archaeological sites [60–62]). L.T. Dolphin and colleagues were the first to use GPR in the field of archeology in 1977 to explore underground caves in New Mexico [63]. In 1982, C. J. Vaughn identified 16th century features at a Basque whaling site in Canada using GPR [56]. Software advances in the 1990s and 2000s led to the development of processing tools that allow for horizontal depth slicing and 3D imaging of GPR data [64]. In the southeastern United States, research-driven geoarchaeological investigations employing GPR (along with other remote sensing techniques) have been focused mainly on historic (e.g., [65–69]), Mississippian and/or Protohistoric (e.g., [70–76]), and Woodland (e.g., [70,72,77,78]) sites. Geophysical investigations in the southeast have rarely been focused solely on Archaic sites ([79] is a notable exception). This is partially because robust features such as structures, villages, and palisades are rarely present at Archaic (and Paleoindian) sites. Fortunately, many of these locations, including David Crockett Birthplace State Park, contain evidence of thousands of years of indigenous occupation (including Archaic) due to the suitability of the landscape for human habitation (e.g., [70,80]). One major advantage of using GPR at these sites is that the GPR signal can penetrate deep enough to reach older layers that may be out of reach for other geophysical methods. Even if these layers are not targeted for excavation, they are still recorded in the geophysical data. Another advantage of geophysical techniques in general is that known sites can be revisited and explored without breaking ground. When used in tandem, archaeological excavations and geophysical investigations enhance both the archaeological record and knowledge of geophysical practice, allowing investigators to not only pinpoint features, but answer research questions and develop new ones [60–62,77,81–83].

2. Materials and Methods

2.1. Geophysical Survey

A geophysical survey of the park was completed in an area encompassing 2 hectares, which was being reconstructed into a historically accurate late 18th-century homestead. This was performed using a GSSI SIR-4000 unit with a 400 MHz antenna. The parameters were as follows: meters per mark = 1, ns time window = 50, sample/scan = 512, and scans/m = 100. The magnetometry survey was conducted with a Bartington Grad 601-2 Magnetic Gradiometer System containing two Grad-01-1000L sensors and a DL601 data logger. A grid network was created using a Real-Time Kinematic (RTK) GNSS, a Spectra Precision SP80 survey kit with a positional accuracy level of ± 0.05 m. Grids measured 30×30 m where possible and were surveyed north to south in a zig-zag pattern, starting in the southwest corner, and with survey lines spaced 0.5 m apart. Survey grid coordinates were recorded with a handheld data collector using *SurveyPro* software. A high-resolution digital orthomosaic created from Unmanned

Aerial Vehicle (UAV) photos within *Agisoft PhotoScan* was used as an additional basemap. A workflow chart of the GPR data processing and OBIA steps is presented in Figure 2.

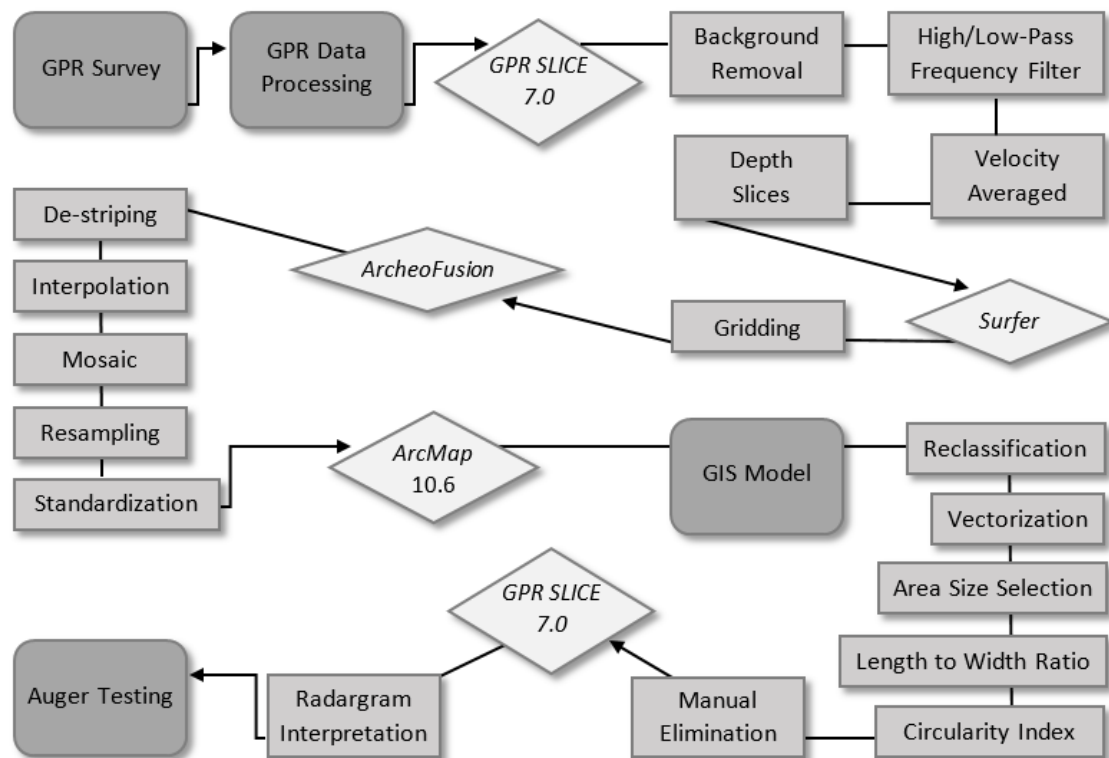


Figure 2. Workflow chart showing steps of Ground-Penetrating Radar (GPR) data processing and object-based image analysis (OBIA) GIS model.

2.2. Ground-Penetrating Radar Data Processing

GPR-SLICE 7.0 was used to process and display the GPR data. Transects were displayed as radargrams showing profiles of depth levels starting at ground surface and ending at less than 2 m. Background removal and bandpass frequency filters were applied to all radargrams and the first break was used to set time zero. Slices and radargrams were examined at varying depth levels for reflections (see Figure 3) that had the potential to be archaeological features. A few of these (see Figure 4) were selected for ground truthing through both augering and excavation test units. Feature depth measurements made during excavation were used to calculate an average velocity of 0.78 m/ns for the archaeological layers, and this was used to export 22 horizontal amplitude depth slices with a thickness of 2.05 ns. Slices were gridded in *Surfer* software using the nearest neighbor method to avoid interpolation errors. *Archeofusion* software was used to mosaic the surfer ASCII grid slices by matching adjacent grids based on regional statistical means. Slice mosaics were georeferenced in *Archeofusion* using the geodetic coordinates of the local site datum and applying an azimuth rotation. Slice mosaics were further processed in *Archeofusion* to remove spikes by using a standard deviation threshold moving window filter and a mean profile filter. Lastly, these mosaics were resampled to a pixel size of 0.125 m × 0.125 m and standardized with a mean of zero and a standard deviation of one.

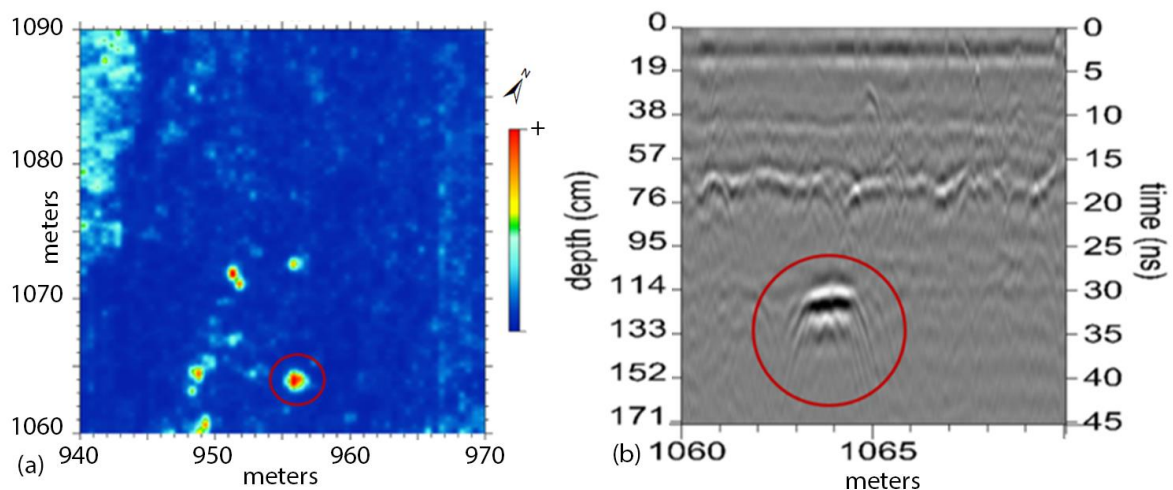


Figure 3. (a) Horizontal GPR Slice 15 of Grid C13 showing an excavated Archaic hearth at 1.02 m below surface (BS); (b) A portion of Radargram 33 showing the hearth's reflection pattern. Smaller hyperbolae representing multiple stacks of fire-cracked rock can be seen below the large flat hyperbola that represents the circular hearth as a whole.

2.3. Archaeological Excavation

The deep anomaly discovered in Radargram 33 of Grid C13 was pinpointed for archaeological testing, and a 1×1 m unit was placed above the feature. At 1.02 m BS, a large circular hearth (Figure 5) consisting of fire-cracked rock (FCR) was uncovered with a diameter greater than one meter. Chert and quartzite lithic debris were recovered through wet screening of sediment located within the hearth layer using a 1/16th inch mesh screen. Ash and wood charcoal were also recovered, and one wood charcoal sample from this level was analyzed by Direct AMS laboratories. The results of the Accelerator Mass Spectrometry (AMS) radiocarbon dating gives an uncalibrated mean (1-sigma) of $> 8083 \pm 40$ BP (D-AMS 033192) with a 2-sigma calibrated age range of 7019–6832 cal BC. The calibration range was generated using *OxCal* 4.3 online software [84] with the IntCal 13 curve for the Northern Hemisphere [85]. Several cultural levels were examined within the geophysical data and identified during the archaeological investigations, including Woodland features and artifacts encountered at depth levels ranging from 0.36 to 0.55 m BS. The remnants of a partially burned Mississippian/Protohistoric structure were uncovered at 0.30 m BS at the base of the plowzone. Diagnostic artifacts from the house floor included broken vessel fragments and three European glass trade beads. AMS radiocarbon dates (Table 1) were obtained from organic material at all cultural levels.

Table 1. Summary of Accelerator Mass Spectrometry (AMS) Radiocarbon Dates.

Sample ID	Charcoal	Test Unit	Feature	Depth m BS	Uncalibrated ($\sigma = 1$)	Calibrated Range ($\sigma = 2$)
D-AMS 033192	Wood	5	3	1.02–1.20	8083 BP \pm 40	7019–6832 cal BC
D-AMS 033776	Wood	36	10	0.30–0.36	1646 BP \pm 31	cal AD 272–534
D-AMS 033773	Wood	46	13	0.35–0.73	1568 BP \pm 26	cal AD 420–550
D-AMS 033775	Wood	ET4	8	0.34–0.45	1534 BP \pm 27	cal AD 460–594
D-AMS 033772	River Cane	7	floor	0.32	282 BP \pm 27	cal AD 1502–1792
D-AMS 033190	Hickory Nut	20	6	0.32	280 BP \pm 27	cal AD 1599–1794
D-AMS 033774	Hickory Nut	20	6	0.32	260 BP \pm 24	cal AD 1572–1799
D-AMS 033191	Wood	4	2	0.55	242 BP \pm 27	cal AD 1555–1800

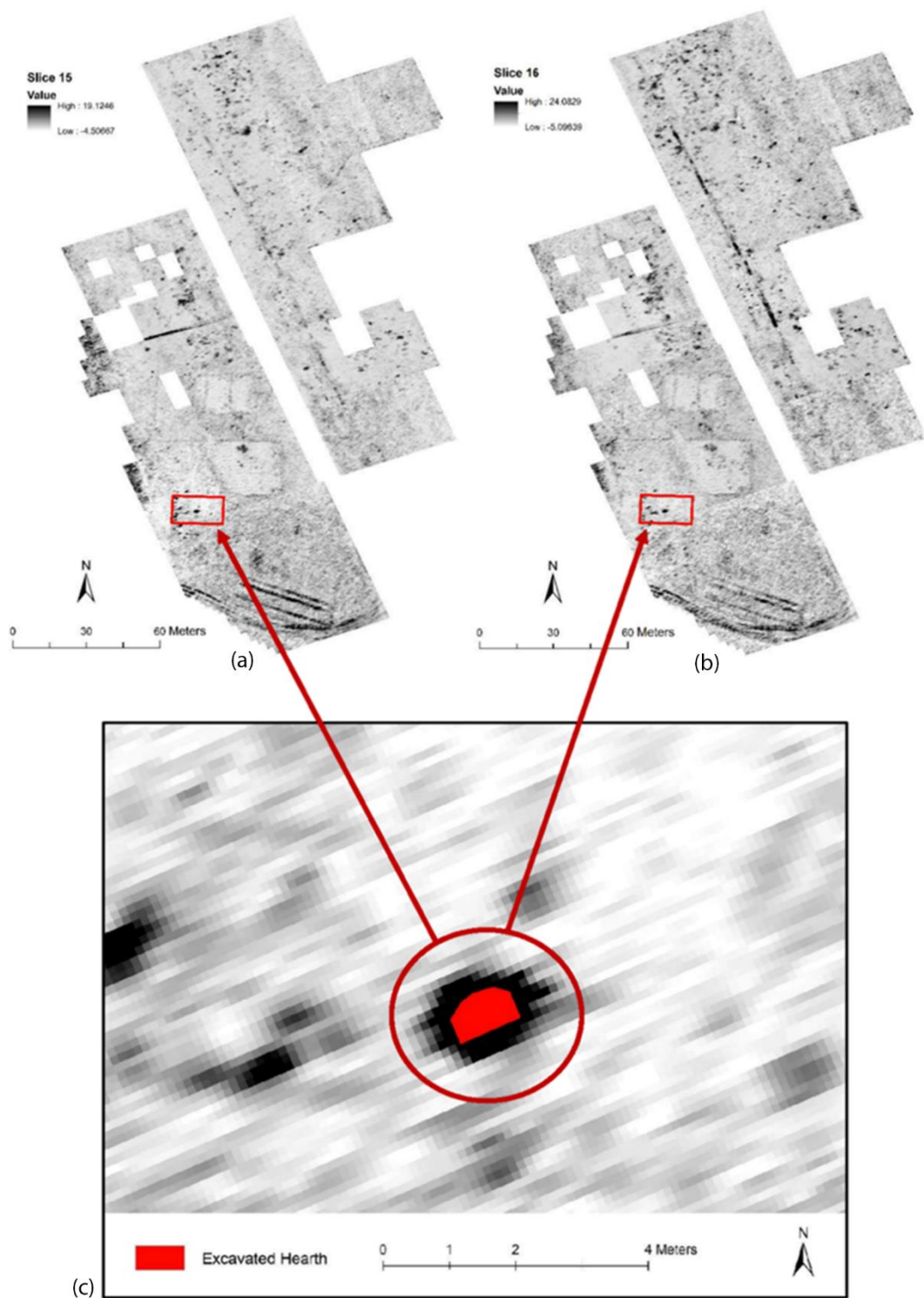


Figure 4. GPR slice mosaics showing the hearth excavation area: (a) Slice 15; (b) Slice 16; (c) Close-up of anomaly in Slice 15 with the red polygon representing the excavated hearth extent recorded by the Real-Time Kinematic (RTK) Global Navigation Satellite Systems (GNSS). GPR slice resolution is 0.125×0.125 m.



Figure 5. (a) Planar view of Test Unit 5, showing the top of the Archaic hearth; (b) Profile view of the hearth, which continued into the unit walls and was not fully excavated. A sterile layer was reached at 1.20 m BS. Dark organic bands can be seen at the hearth level and at 0.55 m BS, which contained probable Woodland remnant hearths in adjacent test units.

2.4. Object-Based Image Analysis

ESRI *ArcMap* software (version 10.6.1) was used to conduct the OBIA on the final processed GPR slice mosaics. Three slice mosaics (Slices 14, 15, and 16) were chosen with a depth range of approximately 0.20 m above and below the level of the excavated hearth. The raster datasets were imported in their original plane coordinates in order to retain exact pixel values that can be slightly altered due to automatic resampling associated with georeferencing. Each slice mosaic was reclassified into a binary image using a global threshold of two standard deviations. Next, a raster to vector conversion was performed to create polygons of the anomalies that had a reflectance value of 2σ or greater. Geometric attributes of the Archaic hearth excavated by the East Tennessee State University (ETSU) team, and hearths previously excavated and recorded by Benthall [40] were used to define probable hearth metrics and extract similar polygons. The OBIA used the following attributes: area, perimeter, L2W ratio, and circularity index. Perimeter and area values were automatically generated through the vector conversion tool. All documented Archaic hearths had diameters ranging from one to two meters, which corresponds to areas between 0.8 and 3.5 m² (see Equation (1)).

Area Selection Formula:

$$(Area \geq 0.8) \text{ AND } (Area \leq 3.5) \quad (1)$$

The L2W ratio was created using the major and minor axis of the polygons with a minimum of 1.0 representing a perfect circle. Polygons were selected with an L2W ratio of less than 2.5 (Equation (2)) to allow room for potential hearths that may be more elliptical in shape, as was seen in Woodland layers during the ETSU excavation and Archaic hearths that were recorded by Benthall [40].

Length-to-Width Ratio:

$$(L/W) \leq 2.5 \quad (2)$$

Several Circularity Index formulas have been developed to calculate a mathematical value indicating deviation from a perfect circle [16,18]. The circularity formula used in this study was obtained from a GEOBIA sinkhole study conducted by Doctor and Young [15]. In this formula, P_o represents the observed or known perimeter of the shape, while P_e represents the expected perimeter value if the shape was a perfect circle (Equation (3), where A = area). The Circularity Index of a perfect circle would be 1.0; all other shapes have a ratio greater than 1.0. A final classification of the polygons was selected using a Circularity Index of less than and equal to 2.0.

Circularity Index:

$$Circ\ i < = 2.0 \quad (3)$$

$$Circ\ i = ((Po - Pe)/Pe) + 1 \quad (4)$$

$$Pe = 2\pi (\sqrt{A}/\pi) \quad (5)$$

All polygons were evaluated by human interpretation to eliminate false positives and clutter from modern features such as utility lines, roads, gardens, and tree roots. Next, they were matched to their location in radargrams, and probable Archaic hearths were identified using expert judgment. Some features had ambiguous GPR reflections indicating possible prehistoric burials and modern utility lines, so these were excluded at this stage.

3. Results

3.1. GIS Model

Incremental model results are presented in Table 2. A combined total of 8344 objects were created from Slices 14, 15, and 16 after segmentation by the global threshold. The OBIA steps radically reduced clutter from modern features by removing polygons outside the prescribed geometric ranges. The area metric reduced the number of polygons by 95%, eliminating many unwanted features such as small reflections created from the recently tilled gardens. The L2W ratio eliminated linear polygons, many of which were reflections from utility lines, ditch lines, and roads. The Circularity Index extracted features that were closer to the shape of a circle, eliminating irregular features such as tree roots. Overall, the automated OBIA steps reduced the total number of polygons by 98%. Further manual elimination of 31 objects was necessary to remove remaining clutter. The remaining 106 objects were matched to corresponding radargrams and expert judgment was employed to identify 18 polygons as probable Archaic hearths containing FCR. Two of the polygons in Slices 15 and 16 were identified as the hearth excavated by the ETSU team, while two more anomalies had overlapping polygons in Slices 14 and 15. Combining these reduced the number of probable hearths to 14. Expert judgment of radargrams also identified four additional reflection patterns as probable hearths, even though they had previously been eliminated. Two were too small, one too large, and the fourth was located at 1.40 m BS—deeper than allowed in the model. The final number of probable Archaic hearths was therefore 17, which is inclusive of the slightly under- and over-sized candidates but excluding the deep one because that GPR slice (Slice 18) was not used in the model. Figures 6–8 show examples of probable Archaic hearths at varying depth levels of Slices 14, 15, and 16 as they appear in (a) radargrams and (b) amplitude depth slices, along with (c) maps of objects extracted by global threshold segmentation, and (d) after OBIA metrics and manual elimination.

Table 2. Anomaly Reduction Steps by Order.

GPR Slice Mosaic	1. Polygons by Reclassification Threshold of 2σ	2. Polygons by Area ($> = 0.8\text{ m}^2$) & ($< = 3.5\text{ m}^2$)	3. Polygons by L2W Ratio ($< = 2.5$)	4. Polygons by Circularity Index ($< = 2$)	5. Modern Feature Elimination	6. Radargram Interpretation for Auger Tests
14	2270	91	68	40	31	7
15	2862	107	71	44	36	5
16	3212	199	91	53	39	6
Total	8344	397	230	137	106	16 (2 overlapping)

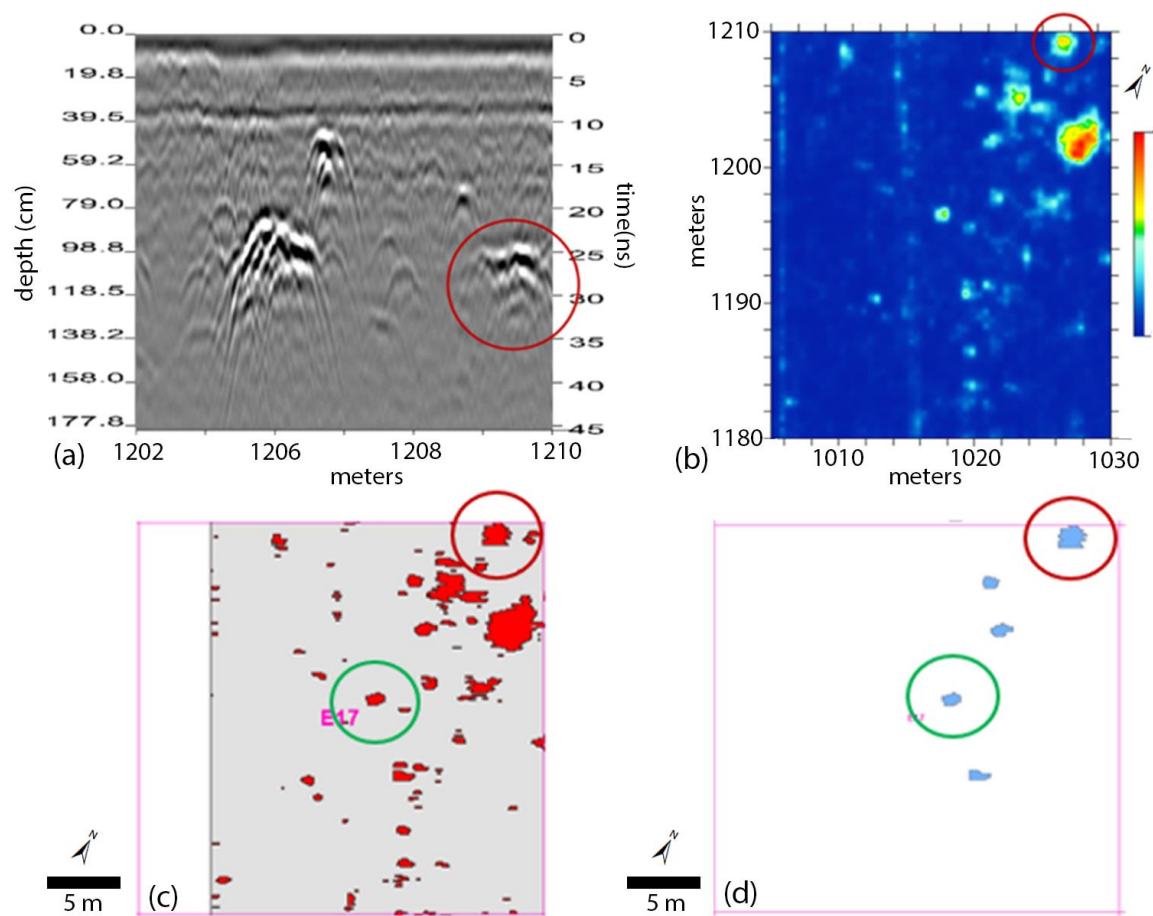


Figure 6. Four views of a probable Archaic hearth (circled in red) in Grid E17 extracted by the semi-automated OBIA model: (a) The reflection pattern in a portion of Radargram 44; (b) GPR Slice 14; (c) Map of objects extracted by global threshold segmentation; (d) Map of objects remaining after manual elimination of noise. Another probable hearth (circled in green) was identified and confirmed at a depth of 1.02 m BS during the auger testing.

3.2. Auger Testing

The 17 probable Archaic hearths were tested with a four-inch (0.1-m) bucket auger. FCR was reached at the approximate predicted depths in 16 of the tests. Radargrams for probable hearths are shown in Figure 9, and corresponding auger test results in Table 3. Probable Hearth 8 did not contain FCR but was interpreted as a prehistoric pit based on the presence of ash, charcoal, and a lithic flake from 0.90 to 1.30 m BS. The pit feature had been previously excluded from the model based on area values greater than the metrics allowed, but it was added back during expert interpretation of radargrams. When obstructions were reached in three of the auger tests, they were moved 0.30 m grid north. Control tests were performed to depths of 1.40 m, at a range of 0.50 to 4 m outside of five of the test feature locations. There was no evidence of FCR in four of the control tests. FCR was reached at 0.99 m BS in one control test placed 0.5 m outside a probable hearth found at 0.92 m BS, which was likely a continuation of the same hearth. The automated OBIA model successfully predicted 15 out of the 17 probable hearths identified by geometry attributes. Probable hearths 4 and 12 had been added based on expert judgment and tested positive for FCR—both were slightly smaller than allowed by the area metric. Figure 10 uses Slice 14 to illustrate how the semi-automated OBIA approach selected thousands of objects and reduced them to 10 probable hearths for that depth interval. Figure 11 shows the location of all Archaic hearths confirmed by the presence of FCR, showing that they occur in a clustered arrangement across the survey area.

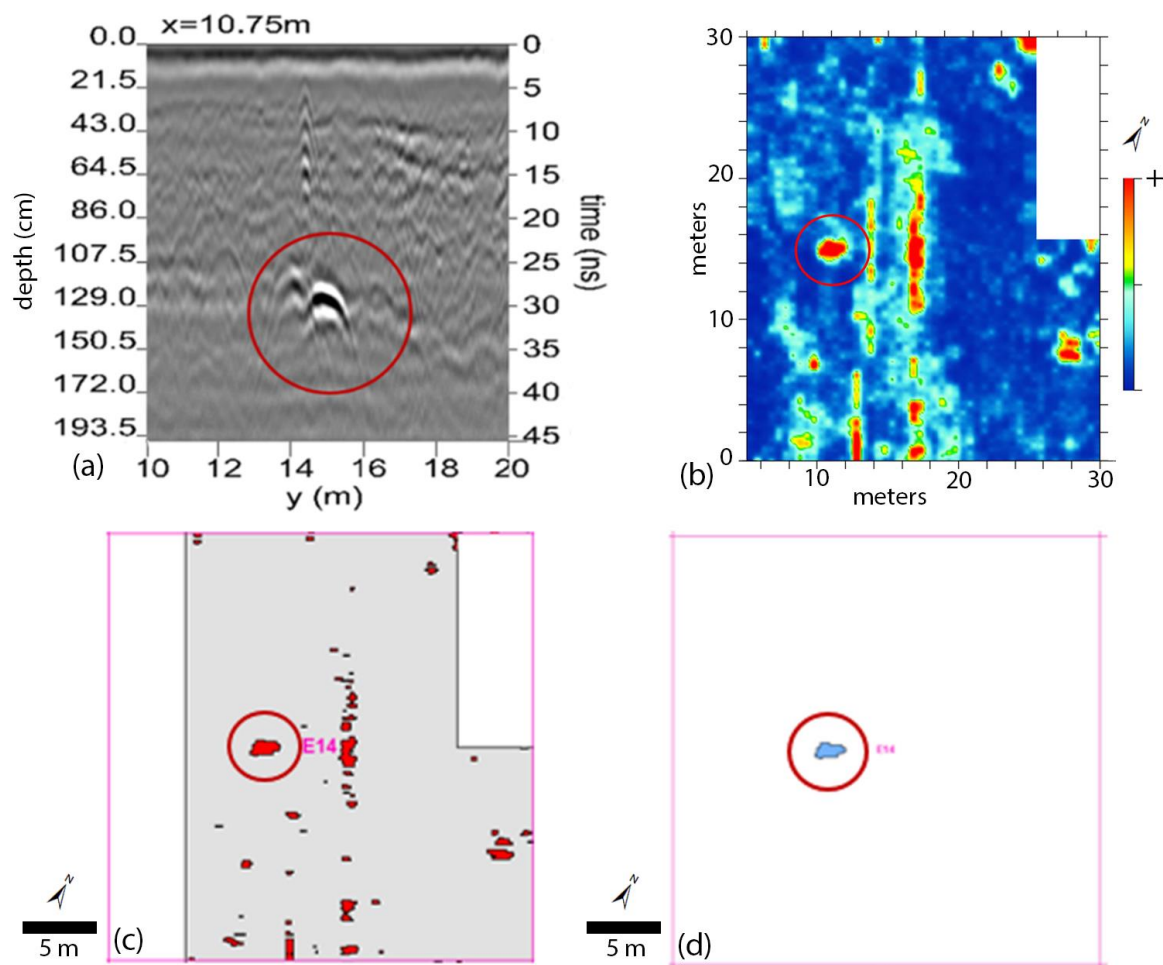


Figure 7. Four views of a probable Archaic hearth (circled in red) in Grid E14, which was confirmed by fire-cracked rock (FCR) in the auger at 1.05 m BS: (a) Reflection pattern in a portion of Radargram 12; (b) GPR Slice 15, where linear features from an electrical line and ditch are also visible; (c) Map of objects after global threshold segmentation; (d) Map of objects remaining after OBIA and manual elimination.

Table 3. Auger and Excavation Test Results

Probable Hearth	Test Number	Predicted m BS	Actual m BS	Predicted in Model	Tested Positive for FCR
1	Excavated Hearth	1.10	1.02	Yes	Yes
2	C13.S14.2/S15.1	0.95	0.92	Yes	Yes
3	C13.S14.3/S15.2	1.02	0.92	Yes	Yes
4	C14.S14.NM1	1.02	0.91	No	Yes
5	D15.S16.1	1.20	1.10	Yes	Yes
6	D15.S16.5	1.15	1.20	Yes	Yes
7	E14.S15.1	1.00	1.05	Yes	Yes
8	E15.S14.NM2	0.95	0.90–1.30	No	No
9	E17.S14.2	0.90	1.02	Yes	Yes
10	E17.S14.6	0.90	0.85	Yes	Yes
11	E17.S16.1	1.12	1.18	Yes	Yes
12	E17.S16.NM3	1.25	1.08	No	Yes
13	E18.S14.2	0.95	1.02	Yes	Yes
14	E18.S14.4	0.85	0.92	Yes	Yes
15	E18.S15.5	0.90	0.94	Yes	Yes
16	F14.S14.4	0.98	1.10	Yes	Yes
17	F14.S16.3	1.20	1.20	Yes	Yes
18	F18.S16.1	0.95	0.87	Yes	Yes

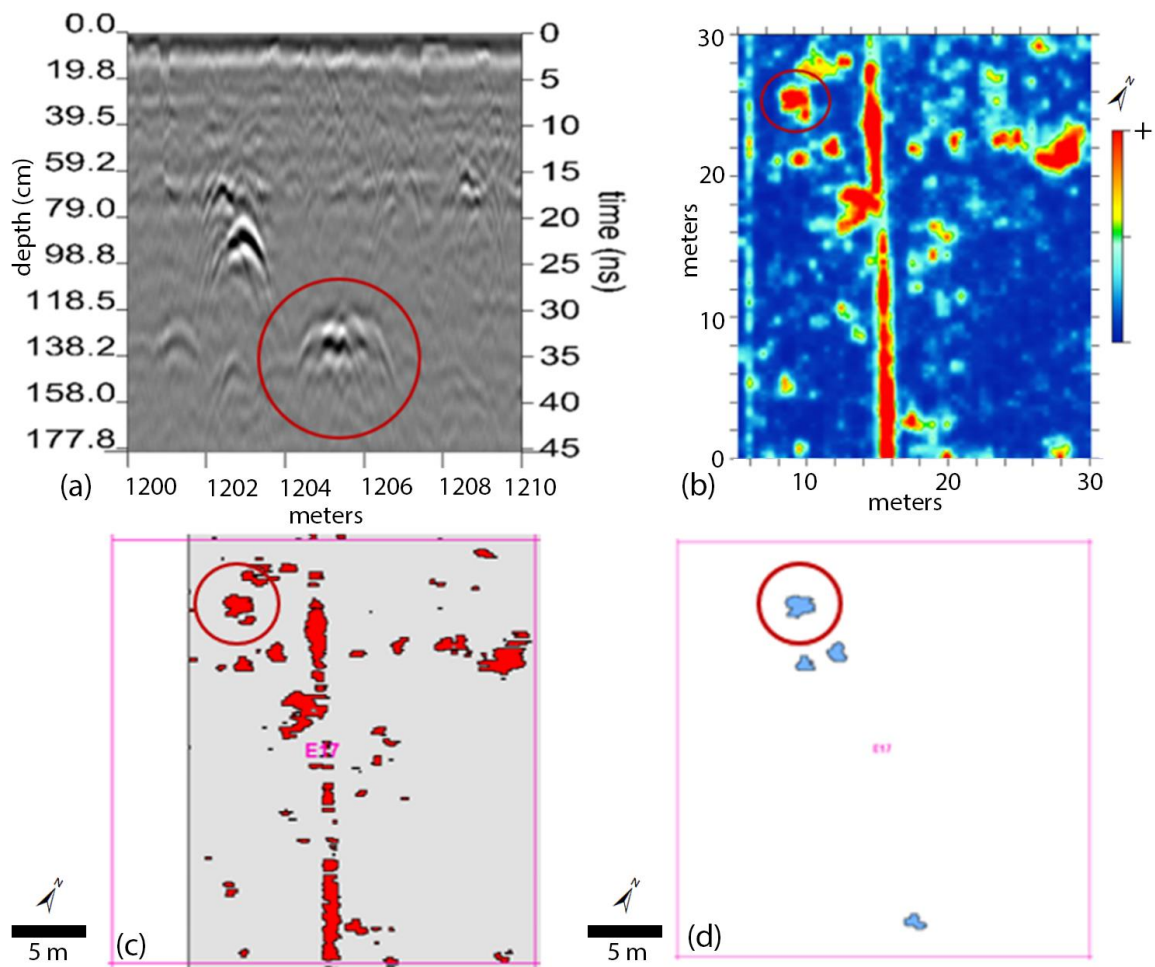


Figure 8. Four views of a probable hearth (circled in red) in Grid E17, which was confirmed by FCR in the auger at 1.18 m BS: (a) Reflection pattern in a portion of Radargram 8; (b) GPR Slice 16, where linear features from a known electrical line are also clearly visible; (c) Map of objects after global threshold segmentation; (d) Map of objects remaining after the OBIA and manual elimination.

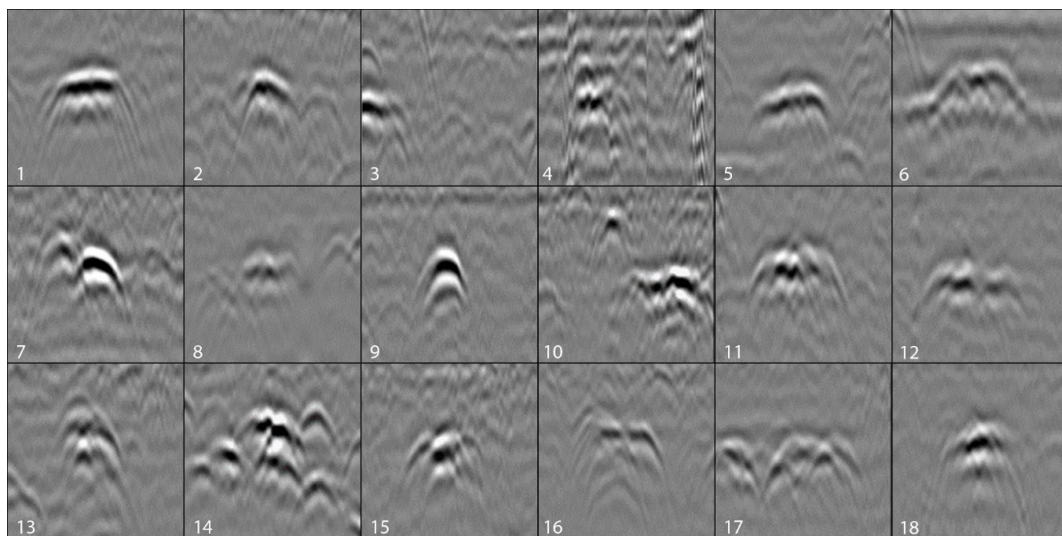


Figure 9. Radargrams showing probable Archaic hearth reflection patterns, which correspond to test results shown in Table 3.

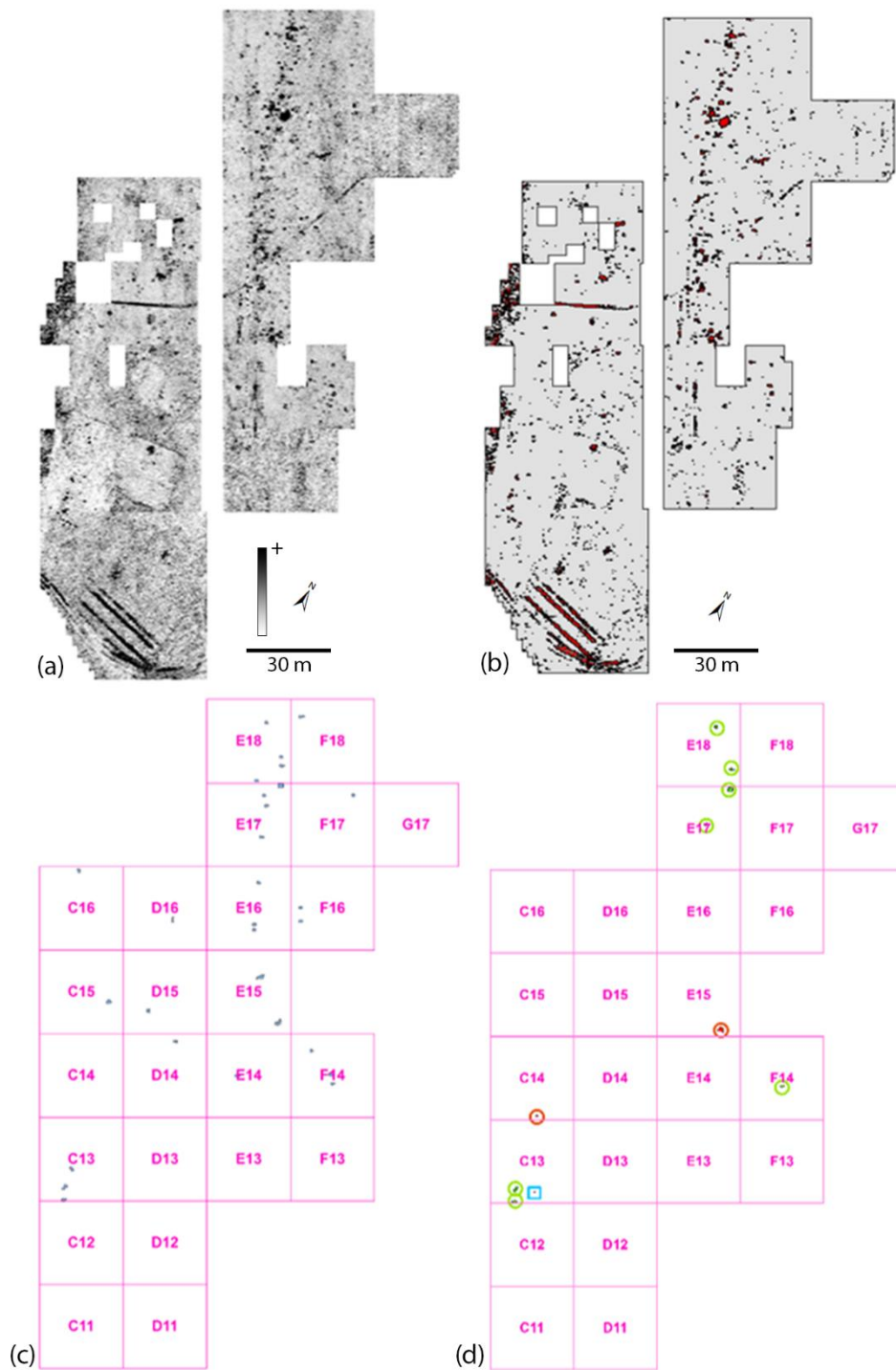


Figure 10. Example of the semi-automated OBIA approach applied to GPR Slice 14. (a) Processed sitewide slice mosaic; (b) Map of objects isolated by global threshold segmentation; (c) Map of 31 objects remaining after applying OBIA metrics and manual elimination; (d) Anomalies tested after human interpretation of radargrams where seven (green circles) were selected by OBIA and tested positive for FCR, two (red circles) were originally excluded due to size but identified as probable hearths during the human interpretation, and one (blue square) represents the top of the excavated archaic hearth and was selected by OBIA in Slice 15 and Slice 16.



Figure 11. Probable Archaic hearths consisting of FCR confirmed by auger testing or excavation. The basemap is a digital orthomosaic created from Unmanned Aerial Vehicle (UAV) imagery. Noticeable patterns of clustering by depth and proximity are visible.

4. Discussion

The results of geophysical surveys vary due to site conditions and feature characteristics. In this case study, deep features were identified within the GPR data that were not found with magnetometry. This was more than likely due to soil conditions and interference from modern noise within the survey area. A micaceous sandy loam was found at all levels of auger testing that reached a depth of 1.40 m. The low conductivity of sandy sediments likely allowed for greater GPR depth penetration, and this seems to have played a role in the ability of the GPR survey to receive strong reflections from features

found at levels below one meter. Modern features affected both the magnetometry and GPR data, especially at levels closer to the ground surface. The survey area contained metallic debris, electrical utility boxes, and a large metal pylon supporting high-powered electrical lines, all of which masked magnetometry readings from more subtle archaeological features. Still, in limited regions with little to no modern magnetic interference, hearths identified by GPR were not detected by magnetometry. This suggests that the hearths do not have magnetic fields strong enough to be detected at these depths.

The OBIA model radically reduced clutter in the GPR data and successfully extracted probable archaeological features. Human interpretation and expert judgment were imperative to delineate all possible Archaic hearths from the GPR data, while excluding features such as utility lines and possible prehistoric burials. Manual examination of radargrams and auger testing also proved that the OBIA excluded some probable hearths; however, this could be corrected by expanding the metrics of the model. Further examination of the radargrams and amplitude depth slices also showed that one probable hearth (Probable Hearth 12 in Figure 9) not included by the OBIA had been separated into smaller polygons due to gaps in the reflectance of the anomalies, reinforcing the need for human interpretation. This problem could also be solved by adding a buffer or proximity analysis to the OBIA steps. All features that were selected by the OBIA and expert judgment tested positive for evidence of human occupation, with many containing charcoal and ash. The success of the OBIA was in part due to the size, shape, and depth of the Archaic features, along with knowledge of the attributes of previously excavated hearths. It is important to note that this type of analysis may not be suitable for all data. As stated by Verdonck et al. [3], 'Where the archaeological features belong to one class with a simple shape (e.g., circular structures), relatively simple algorithms can be used.'

The map of the auger-tested probable hearths (Figure 11) shows noticeable patterns of clustering by depth and proximity, which may indicate seasonal occupation of small groups. Resources such as nearby springs were more than likely utilized, along with a local abundance of small and large game and freshwater species from the adjacent creek and river [40]. The quartzite and chert debris found during the excavation of the Archaic hearth suggests stone tool production and possible local raw material procurement, an idea previously proposed about this site by Benthall [40]. Additional AMS radiocarbon dating of charcoal samples may help determine a more robust occupation range. However, it is impossible to know the true nature of the occupation without a more extensive archaeological investigation. The FCR of the ETSU-excavated Archaic hearth was stacked at a height of greater than 0.10 m and was mounded in the center. Overall, the tested features were reached at depth levels ranging from 0.85 to 1.20 m BS, and exact occupation levels cannot be determined from auger testing alone. The survey area of the park is relatively flat due to decades of plowing and grading associated with modern construction. The slope and elevation of the prehistoric landscape and river terrace may have been dramatically different during the Archaic Period. Landscape changes and feature disturbance are particularly likely given the proximity to the meandering Nolichucky River and associated flooding.

5. Conclusions

Semi-automated OBIA can be utilized to quickly delineate homogenous subsurface archaeological features from preprocessed geophysical data. This method was successfully applied to extract Archaic hearths from a large GPR dataset using parameters of known Archaic hearths. A logical sequence was constructed employing computer-generated algorithms within GIS software to eliminate clutter. The result was a time-saving approach that reduced the number of anomalies by over 98% and eliminated some of the subjectivity and inconsistency associated with manual interpretation. Expert judgment, excavation, and auger tests were used to validate the model, resulting in the identification of 17 probable Archaic hearths, of which 15 were successfully predicted by OBIA. This method could be beneficial in processing large datasets where homogeneous features are expected to be found within geophysical data. OBIA could also be enhanced by future software development that would allow the technique to be implemented on anomalies found within GPR radargrams and 3D geophysical data. OBIA was implemented to target deep Archaic features that are sometimes overlooked, ignored,

or not identified with geophysical techniques having more limited depth capabilities. The OBIA of the preprocessed data was completed for one mosaic dataset in under 20 min, and while additional time was needed for human interpretation, the selected anomalies were quickly pinpointed within GPR radargrams. Auger testing was a fast and suitable method, as FCR could be felt and heard (and sometimes retrieved) without the need for a full excavation, while still collecting sediment samples and cultural material. Possible occupation patterns were seen through GIS mapping of the probable Archaic hearth locations, adding to the archaeological record of the park and region. By combining GPR, GIS, OBIA, expert judgment, limited excavation, and auger testing, a cost-effective and labor-efficient method was developed that could be utilized to discover similar cultural components at local and regional prehistoric sites and adapted for other feature types and sites worldwide.

Author Contributions: Conceptualization, E.G.E.; methodology, R.L.C. and E.G.E.; software, R.L.C. and E.G.E.; validation, R.L.C. and E.G.E.; formal analysis, R.L.C.; investigation, R.L.C. and E.G.E.; resources, E.G.E.; data curation, R.L.C.; writing—original draft preparation, R.L.C.; writing—review and editing, R.L.C. and E.G.E.; visualization, R.L.C. and E.G.E.; supervision, E.G.E.; project administration, R.L.C. and E.G.E.; funding acquisition, R.L.C. and E.G.E. All authors have read and agreed to the published version of the manuscript.

Funding: This research was funded in part by the Tennessee State Historical Commission through a Historic Preservation Survey & Planning Grant entitled *Geophysical Survey at David Crockett Birthplace State Park, Greene County, TN* (2018). The activity that is the subject of this publication has been financed in part with federal funds from the National Park Service. However, the contents and options do not necessarily reflect the views or policies of the Department of the Interior, nor does the mention of trade names or commercial products constitute endorsement or recommendation by the Department of the Interior. Regulations of the U.S. Department of Interior strictly prohibit unlawful discrimination in departmental Federally Assisted Programs on the basis of race, color, national origin, age or handicap. Any person who believes he or she has been discriminated against in any program, activity, or facility operated by a recipient of Federal assistance should write to: Director, Equal Opportunity Program, U.S. Department of the Interior, National Park Service, P.O. Box 37127, Washington D.C. 20013-7127. The Article Processing Charge for publication of this work was funded in part by a grant from the East Tennessee State University Research Development Committee Small Grants Program.

Acknowledgments: We would like to thank the Tennessee Division of Archaeology and the Tennessee State Park Systems for their continuing support. We are grateful for assistance from the East Tennessee State University Geosciences and Sociology & Anthropology Departments, especially Jay Franklin, Chris Widga, and William Duncan. We would also like to acknowledge the many students, volunteers, and professionals that made this project possible, especially local expert S.D. Dean. Permit number 000958R was granted by the State of Tennessee Department of Environment and Conservation through the Division of Archaeology. Last, we would like to thank the three anonymous reviewers for their critical insight and recommendations that led to the enhancement and clarification of this manuscript.

Conflicts of Interest: The authors declare no conflict of interest. The funders had no role in the design of the study; in the collection, analyses, or interpretation of data; in the writing of the manuscript, or in the decision to publish the results.

References

1. Barceló, J.A. The birth and historical development of computational intelligence applications in archaeology. *Archeol. e Calcolatori* **2009**, *20*, 95–109.
2. Puyol-Gruart, J. Computer science, artificial intelligence and archaeology. *BAR Int. Ser.* **1999**, *757*, 19–28.
3. Verdonck, L.; De Smedt, P.; Verhegge, J. Making sense of anomalies: Practices and challenges in the archaeological interpretation of geophysical data. In *Innovation in Near-Surface Geophysics*, 1st ed.; Persico, R., Piro, S., Linford, N., Eds.; Elsevier: Amsterdam, The Netherlands, 2019; pp. 151–194. [[CrossRef](#)]
4. Blaschke, T. Object based image analysis for remote sensing. *ISPRS J. Photogramm. Remote Sens.* **2010**, *65*, 2–16. [[CrossRef](#)]
5. Blaschke, T.; Kelly, M.; Merschdorf, H. Object-based image analysis: Evolution, history, state of the art, and future vision. In *Remotely Data Characterization, Classification, and Accuracies*; Thenkabil, P.S., Ed.; CRC Press: Boca Raton, FL, USA, 2015; Volume 1, pp. 277–293. [[CrossRef](#)]
6. Kamagata, N.; Akamatsu, Y.; Mori, M.; Li, Y.Q.; Hoshino, Y.; Hara, K. Comparison of pixel-based and object-based classifications of high resolution satellite data in urban fringe areas. In *Proceedings of the 26th Asian Conference on Remote Sensing*, Hanoi, Vietnam, 7–11 November 2005; Curran Associates, Inc.: Red Hook, NY, USA, 2005; Volume 3, pp. 1590–1595.

7. Liu, D.; Xia, F. Assessing object-based classification: Advantages and limitations. *Remote Sens. Lett.* **2010**, *1*, 187–194. [[CrossRef](#)]
8. Sevara, C.; Pregesbauer, M.; Doneus, M.; Verhoeven, G.; Trinks, I. Pixel versus object—A comparison of strategies for the semi-automated mapping of archaeological features using airborne laser scanning data. *J. Archaeol. Sci. Rep.* **2016**, *5*, 485–498. [[CrossRef](#)]
9. Sibaruddin, H.I.; Shafri, H.Z.M.; Pradhan, B.; Haron, N.A. Comparison of pixel-based and object-based image classification techniques in extracting information from UAV imagery data. In *IOP Conference Series: Earth and Environmental Science*; IOP Publishing: Bristol, UK, 2018; Volume 169, p. 012098. [[CrossRef](#)]
10. Verhagen, P.; Drăguț, L. Object-based landform delineation and classification from DEMs for archaeological predictive mapping. *J. Archaeol. Sci.* **2012**, *39*, 698–703. [[CrossRef](#)]
11. Xiaoxia, S.; Jixian, Z.; Zhengjun, L. *A Comparison of Object-Oriented and Pixel-Based Classification Approaches Using Quickbird Imagery*; Chinese Academy of Surveying and Mapping: Beijing, China, 2004.
12. Kvamme, K. An Examination of Automated Archaeological Feature Recognition in Remotely Sensed Imagery. In *Computational Approaches to Archaeological Spaces*; Andrew, B., Lake, M., Eds.; Left Coast Press: Walnut Creek, CA, USA, 2013; pp. 53–68.
13. Luo, L.; Wang, X.; Guo, H.; Lasaponara, R.; Zong, X.; Masini, N.; Wang, G.; Shi, P.; Khatteli, H.; Chen, F.; et al. Airborne and spaceborne remote sensing for archaeological and cultural heritage applications: A review of the century (1907–2017). *Remote Sens. Environ.* **2019**, *232*, 111280. [[CrossRef](#)]
14. Minár, J.; Evans, I.S. Elementary forms for land surface segmentation: The theoretical basis of terrain analysis and geomorphological mapping. *Geomorphology* **2008**, *95*, 236–259. [[CrossRef](#)]
15. Doctor, D.H.; Young, J.A. An Evaluation of Automated GIS Tools for Delineating Karst Sinkholes and Closed Depressions from 1-meter LIDAR-Derived Digital Elevation Data. In Proceedings of the 13th Multidisciplinary Conference on Sinkholes and the Engineering and Environmental Impacts of Karst, Carlsbad, Mexico, 6–10 May 2013; Land, L., Doctor, D.H., Stephenson, J.B., Eds.; National Cave and Karst Research Institute: Carlsbad, NM, USA, 2013; pp. 449–458. [[CrossRef](#)]
16. Kopal, M.; Bertonec, I.; Pirotti, F.; Dakskobler, I.; Kutnar, L. Using lidar data to analyze sinkhole characteristics relevant for understory vegetation under forest cover—Case study of a high karst area in the Dinaric Mountains. *PLoS ONE* **2015**, *10*, e0122070. [[CrossRef](#)] [[PubMed](#)]
17. Parise, M.; Pisano, L.; Zumpano, V. Detection and Characterization of Sinkholes through Integration of Field Surveys and Semi-automated Techniques. In *Eurokarst 2018, Besançon: Advances in the Hydrogeology of Karst and Carbonate Reservoirs*; Springer: Cham, Switzerland, 2020; pp. 3–9. [[CrossRef](#)]
18. Šegina, E.; Benac, Č.; Rubinić, J.; Knez, M. Morphometric analyses of dolines—The problem of delineation and calculation of basic parameters. *Acta Carsologica* **2018**, *47*. [[CrossRef](#)]
19. Shannon, J.C.; Moore, D.; Li, Y.; Olsen, C. LiDAR-based Sinkhole Detection and Mapping in Knox County, Tennessee. *Pursuit J. Undergrad. Res. Univ. Tenn.* **2019**, *9*, 1–23.
20. Verbovšek, T.; Gabor, L. Morphometric properties of dolines in Matarsko podolje, SW Slovenia. *Environ. Earth Sci.* **2019**, *78*, 396. [[CrossRef](#)]
21. Davis, D.S. Object-based image analysis: A review of developments and future directions of automated feature detection in landscape archaeology. *Archaeol. Prospect.* **2019**, *26*, 155–163. [[CrossRef](#)]
22. Davis, D.S.; Sanger, M.C.; Lipo, C.P. Automated mound detection using lidar and object-based image analysis in Beaufort County, South Carolina. *Southeast. Archaeol.* **2019**, *38*, 23–37. [[CrossRef](#)]
23. Freeland, T.; Heung, B.; Burley, D.V.; Clark, G.; Knudby, A. Automated feature extraction for prospection and analysis of monumental earthworks from aerial LiDAR in the Kingdom of Tonga. *J. Archaeol. Sci.* **2016**, *69*, 64–74. [[CrossRef](#)]
24. Vogelaar, C. Using GIS Modelling as a Tool to Search for Late Pleistocene and Early Holocene Archaeology on Quadra Island, British Columbia. Master's Thesis, University of Victoria, Victoria, BC, Canada, 2017.
25. Dawson, R.A.; Petropoulos, G.P.; Toullos, L.; Srivastava, P.K. Mapping and monitoring of the land use/cover changes in the wider area of Itanos, Crete, using very high resolution EO imagery with specific interest in archaeological sites. *Environ. Dev. Sustain.* **2020**, *22*, 3433–3460. [[CrossRef](#)]
26. Hay, G.J.; Castilla, G. Geographic Object-Based Image Analysis (GEOBIA): A new name for a new discipline. In *Object-Based Image Analysis: Spatial Concepts for Knowledge-Driven Remote Sensing Applications*, 1st ed.; Blaschke, T., Lang, S., Hay, G., Eds.; Springer: Berlin/Heidelberg, Germany, 2008; pp. 75–89. [[CrossRef](#)]

27. Al-Nuaimy, W.; Huang, Y.; Nakhkash, M.; Fang, M.T.C.; Nguyen, V.T.; Eriksen, A. Automatic detection of buried utilities and solid objects with GPR using neural networks and pattern recognition. *J. Appl. Geophys.* **2000**, *43*, 157–165. [[CrossRef](#)]
28. Bescoby, D.J.; Cawley, G.C.; Chroston, P.N. Enhanced interpretation of magnetic survey data using artificial neural networks: A case study from Butrint, southern Albania. *Archaeol. Prospect.* **2004**, *11*, 189–199. [[CrossRef](#)]
29. Ernenwein, E.G. Integration of multidimensional archaeogeophysical data using supervised and unsupervised classification. *Near Surf. Geophys.* **2009**, *7*, 147–158. [[CrossRef](#)]
30. Florio, G.; Lo Re, D. Terracing of potential fields by clustering methods. *Geophysics* **2018**, *83*, G47–G58. [[CrossRef](#)]
31. Sheen, N.P.; Aspinall, A. A simulation of anomalies to aid the interpretation of magnetic data. *BAR Int. Ser.* **1995**, *598*, 57–63.
32. Ward, W.O.; Wilkinson, P.B.; Chambers, J.E.; Oxby, L.S.; Bai, L. Distribution-based fuzzy clustering of electrical resistivity tomography images for interface detection. *Geophys. J. Int.* **2014**, *197*, 310–321. [[CrossRef](#)]
33. Hegyi, A.; Vernica, M.M.; Drăguț, L. An object-based approach to support the automatic delineation of magnetic anomalies. *Archaeol. Prospect.* **2019**, *27*, 3–12. [[CrossRef](#)]
34. Pregeßbauer, M.; Trinks, I.; Neubauer, W. An object oriented approach to automatic classification of archaeological features in magnetic prospection data. *Near Surf. Geophys.* **2014**, *12*, 651–656. [[CrossRef](#)]
35. Salguero, F.; Prat, F.; Moreno, F.; Romero, S. Mean shift: A non-parametric algorithm for the segmentation of anomalies in geophysical images obtained from magnetic prospection data. *Archaeometry* **2011**, *53*, 642–659. [[CrossRef](#)]
36. Linford, N.; Linford, P. The application of semi-automated vector identification to large scale archaeological data sets considering anomaly morphology. In Proceedings of the 12th International Conference of Archaeological Prospection, University of Bradford, Bradford, UK, 12–16 September 2017; Jennings, B., Gaffney, C., Sparrow, T., Gaffney, S., Eds.; Archaeopress Archaeology: Oxford, UK, 2017; p. 4919.
37. Schmidt, A.; Tsetsckhladze, G. Raster was yesterday: Using vector engines to process geophysical data. *Archaeol. Prospect.* **2013**, *20*, 59–65. [[CrossRef](#)]
38. Middleton, M.; Schnur, T.; Sorjonen-Ward, P.; Hyvönen, E. Geological lineament interpretation using the object-based image analysis approach: Results of semi-automated analyses versus visual interpretation. In *Geological Survey of Finland, Special Paper 57*; Sarala, P., Ed.; Juvenes Print—Suomen Yliopistopaino Oy: Tampere, Finland, 2015; pp. 135–154.
39. Seijmonsbergen, A.C.; Hengl, T.; Anders, N.S. Semi-automated identification and extraction of geomorphological features using digital elevation data. In *Developments in Earth Surface Processes*; Smith, M.J., Paron, P., Griffiths, J.S., Eds.; Elsevier: Amsterdam, The Netherlands, 2011; Volume 15, pp. 297–335. [[CrossRef](#)]
40. Benthall, J.L. *Archaeological Investigations at Davy Crockett Birthplace Historical Area*; Department of Environment and Conservation, Division of Archaeology: Nashville, TN, USA, 1997; pp. 1–77, Unpublished work.
41. Smith, S.D. *Historical Background and Archaeological Testing of the Davy Crockett Birthplace State Historic Area, Greene County, Tennessee, Research Series No. 6*; Tennessee Department of Conservation: Nashville, TN, USA, 1980; pp. 1–67.
42. Rodgers, J. *Geologic Map of East Tennessee with Explanatory Text*; Bulletin 58, Part II; Tennessee Division of Geology: Nashville, TN, USA, 1953; pp. 1–168.
43. Hardeman, W.D.; Miller, R.A.; Swingle, G.D. *Geological Map of Tennessee*; Tennessee Division of Geology: Nashville, TN, USA, 1966; east sheet.
44. Soil Survey Staff, Natural Resources Conservation Service, United States Department of Agriculture. Web Soil Survey. Available online: <http://websoilsurvey.sc.egov.usda.gov/> (accessed on 5 September 2019).
45. Dalton-Carriger, J.N. New Perspectives on the Seventeenth-Century Protohistoric Period in East Tennessee: Redefining the Period through Glass Trade Bead and Ceramic Analyses. Ph.D. Dissertation, University of Tennessee, Knoxville, TN, USA, 2016; pp. 1–180.
46. Hudson, C.M. *The Southeastern Indians*; University of Tennessee Press: Knoxville, TN, USA, 1976; pp. 34–119.
47. Ward, H.T.; Davis, R.P., Jr. *Time before History: The Archaeology of North Carolina*; The University of North Carolina Press: Chapel Hill, NC, USA, 1999; pp. 1–328.
48. Anderson, D.G.; Sassaman, K.E. Early and middle Holocene periods, 9500–3750 BC. In *Southeast Volume, Smithsonian Handbook of North American Indians*; Fogleson, R.D., Ed.; Smithsonian Institution: Washington, DC, USA, 2004; pp. 87–100.

49. Gibson, J.L. Navels of the Earth: Sedentism in Early Mound-Building Cultures in the Lower Mississippi Valley. *World Archaeol.* **2006**, *38*, 311–329. [[CrossRef](#)]
50. Russo, M. Why we don't believe in Archaic ceremonial mounds and why we should: The case from Florida. *Southeast. Archaeol.* **1994**, *13*, 93–109.
51. Sassaman, K.E.; Rudolphi, W. Communities of practice in the early pottery traditions of the American Southeast. *J. Anthropol. Res.* **2001**, *57*, 407–425. [[CrossRef](#)]
52. McIlhany, C.W. Archaeological Survey of the Middle Nolichucky River Basin of Northeastern Tennessee. Master's Thesis, University of Tennessee, Knoxville, TN, USA, 1978; pp. 1–36, Unpublished work.
53. Tennessee Division of Archaeology (TDOA); Nashville, TN, USA. Personal communication, 2020.
54. Conyers, L.B. *Interpreting Ground-Penetrating Radar for Archaeology*; Left Coast Press: Walnut Creek, CA, USA, 2012; pp. 17–208. [[CrossRef](#)]
55. Dojack, L. *Ground Penetrating Radar Theory, Data Collection, Processing, and Interpretation: A Guide for Archaeologists*; University of British Columbia: Vancouver, BC, Canada, 2012; p. 89. [[CrossRef](#)]
56. Vaughan, C.J. Ground-penetrating radar surveys used in archaeological investigations. *Geophysics* **1986**, *51*, 595–604. [[CrossRef](#)]
57. Neal, A. Ground-penetrating radar and its use in sedimentology: Principles, problems and progress. *Earth Sci. Rev.* **2004**, *66*, 261–330. [[CrossRef](#)]
58. Smith, D.G.; Jol, H.M. Ground penetrating radar: Antenna frequencies and maximum probable depths of penetration in Quaternary sediments. *J. Appl. Geophys.* **1995**, *33*, 93–100. [[CrossRef](#)]
59. Witten, A.J. *Handbook of Geophysics and Archaeology*; Equinox Publishing Limited: London, UK, 2006; pp. 214–271. [[CrossRef](#)]
60. Kvamme, K.L. Geophysical surveys as landscape archaeology. *Am. Antiq.* **2003**, *68*, 435–457. [[CrossRef](#)]
61. Kvamme, K.L. A Decade of Geophysics and Remote Sensing in North American Archaeology: Practices, Advances, and Trends. In *Archaeological Remote Sensing in North America*; McKinnon, D.P., Haley, B.S., Eds.; University of Alabama Press: Tuscaloosa, AL, USA, 2017; pp. 215–266.
62. Thompson, V.D.; Arnold, P.J.; Pluckhahn, T.J.; Vanderwarker, A.M. Situating remote sensing in anthropological archaeology. *Archaeol. Prospect.* **2011**, *62*. [[CrossRef](#)]
63. Vickers, R.S.; Dolphin, L.T.; Johnson, D. Archaeological investigations at Chaco Canyon using subsurface radar. In *Remote Sensing Experiments in Cultural Resource Studies*; Lyons, T.R., Ed.; National Park Service, U.S. Department of the Interior and University of New Mexico: Albuquerque, NM, USA, 1976; pp. 81–101.
64. Ernenwein, E.G.; Kvamme, K.L. Data processing issues in large-area GPR surveys: Correcting trace misalignments, edge discontinuities and striping. *Archaeol. Prospect.* **2008**, *15*, 133–149. [[CrossRef](#)]
65. Chapman, J.K. Comparison of Archeological Survey Techniques at Camp Lawton, a Civil War Prison Stockade. Master's Thesis, Georgia Southern University, Statesboro, GA, USA, 2012.
66. Jones, G. Geophysical investigation at the Falling Creek ironworks, an early industrial site in Virginia. *Archaeol. Prospect.* **2001**, *8*, 247–256. [[CrossRef](#)]
67. Jones, G. Geophysical mapping of historic cemeteries. *Tech. Briefs Hist. Archaeol.* **2008**, *3*, 25–38.
68. Patch, S.M.; Espenshade, C.T.; Lowry, S.; Severts, P. 'No Terms but Unconditional Surrender': Archaeological and Geophysical Assessment of the Fort Donelson Confederate Monument Landscape, Stewart County, Tennessee. *Tenn. Archaeol.* **2015**, *7*, 110–140.
69. Thompson, V.D.; DePratter, C.B.; Thompson, A.D.R. A preliminary exploration of Santa Elena's sixteenth century colonial landscape through shallow geophysics. *J. Archaeol. Sci. Rep.* **2016**, *9*, 178–190. [[CrossRef](#)]
70. Bigman, D.P.; Lanzarone, P.M. Investigating construction history, labour investment and social change at Ocmulgee National Monument's Mound A, Georgia, USA, using ground-penetrating radar. *Archaeol. Prospect.* **2014**, *21*, 213–224. [[CrossRef](#)]
71. Menzer, J.G. Discovering Rock Features with Geophysical Exploration and Archaeological Testing at the Mississippian Pile Mound Site, Upper Cumberland Plateau, Tennessee. Master's Thesis, East Tennessee State University, Johnson City, TN, USA, 2015.
72. McNutt, C.H.; Franklin, J.D.; Henry, E.R. New perspectives on Mississippian occupations in western Tennessee and northwestern Mississippi: Recent chronological and geophysical investigations at Chucalissa (40SY1), Shelby County, Tennessee. *Southeast. Archaeol.* **2012**, *31*, 231–250. [[CrossRef](#)]
73. Moore, P.A. A Geophysical Survey of the Kituhwa Mound (31SW2) and the Surrounding Area (31SW1), Swain County, North Carolina. Ph.D. Dissertation, University of Tennessee, Knoxville, TN, USA, 2009.

74. Patch, S.M.; Lowry, S.; Pritchard, E. Two Examples from the Tennessee River Valley. In *Archaeological Remote Sensing in North America: Innovative Techniques for Anthropological Applications*; McKinnon, D.P., Haley, B.S., Eds.; University of Alabama Press: Tuscaloosa, AL, USA, 2017; p. 28.
75. Seinfeld, D.M.; Bigman, D.P.; Stauffer, J.G.; Nowak, J.C. Mound building at Lake Jackson (8LE1), Tallahassee, Florida: New insights from ground penetrating radar. *Southeast. Archaeol.* **2015**, *34*, 220–236. [[CrossRef](#)]
76. Schubert, A.; Horsley, T. Determining village extent and layout utilizing geophysical survey and excavation at the Mississippian site of Cane River, North Carolina. In Proceedings of the Presented at the 80th Annual Meeting of the Society for American Archaeology, San Francisco, CA, USA, 15–19 April 2015. [[CrossRef](#)]
77. Horsley, T.; Wright, A.; Barrier, C. Prospecting for new questions: Integrating geophysics to define anthropological research objectives and inform excavation strategies at monumental sites. *Archaeol. Prospect.* **2014**, *21*, 75–86. [[CrossRef](#)]
78. Thompson, V.D.; Marquardt, W.H.; Walker, K.J. A remote sensing perspective on shoreline modification, canal construction and household trajectories at pineland along Florida’s southwestern Gulf Coast. *Archaeol. Prospect.* **2014**, *21*, 59–73. [[CrossRef](#)]
79. Hargrave, M.L.; Britt, T.; Reynolds, M.D. Magnetic evidence of ridge construction and use at Poverty Point. *Am. Antiq.* **2007**, *72*, 757–769. [[CrossRef](#)]
80. Thompson, V.D.; DePratter, C.B.; Lulewicz, J.; Lulewicz, I.H.; Roberts Thompson, A.D.; Cramb, J.; Ritchison, B.T.; Colvin, M.H. The archaeology and remote sensing of Santa Elena’s four millennia of occupation. *Remote Sens.* **2018**, *10*, 248. [[CrossRef](#)]
81. Aspinall, A.; Gaffney, C.; Conyers, L.B. Archaeological prospection—The first fifteen years. *Archaeol. Prospect.* **2008**, *15*, 241–245. [[CrossRef](#)]
82. Conyers, L.B. Ground-penetrating Radar for Anthropological Research. *Antiquity* **2010**, *84*, 175–184. [[CrossRef](#)]
83. Conyers, L.B.; Leckebusch, J. Geophysical archaeology research agendas for the future: Some ground-penetrating radar examples. *Archaeol. Prospect.* **2010**, *17*. [[CrossRef](#)]
84. Ramsey, C.B. Bayesian analysis of radiocarbon dates. *Radiocarbon* **2009**, *51*, 337–360. [[CrossRef](#)]
85. Reimer, P.J.; Bard, E.; Bayliss, A.; Beck, J.W.; Blackwell, P.G.; Ramsey, C.B.; Buck, C.E.; Cheng, H.; Edwards, R.L.; Friedrich, M.; et al. IntCal13 and Marine13 radiocarbon age calibration curves 0–50,000 years cal BP. *Radiocarbon* **2013**, *55*, 1869–1887. [[CrossRef](#)]



© 2020 by the authors. Licensee MDPI, Basel, Switzerland. This article is an open access article distributed under the terms and conditions of the Creative Commons Attribution (CC BY) license (<http://creativecommons.org/licenses/by/4.0/>).